SUPPORTING INFORMATION

Thermodynamically stable quasi-liquid interface for dendrite-free sodium metal anodes

Qi Zhang, Min Hu, Jia He, Xizheng Liu, Guang He* and Yi Ding*

Tianjin Key Laboratory of Advanced Functional Porous Materials, Institute for New Energy Materials and Low-Carbon Technologies, School of Materials Science and Engineering, Tianjin University of Technology, Tianjin, 300384, P. R. China.

Correspondence: heguang@tjut.edu.cn, yding@tjut.edu.cn

EXPERIMENTAL SECTION

Synthesis of amalgams: The amalgam-protected anodes were prepared by alloying reactions between mercury-rich amalgam and sodium at room temperature under Ar atmosphere. Specifically, mercury-rich Na-Hg alloys were first synthesized by dissolving desired sodium in mercury (**Caution: the reaction between sodium and mercury is violent due to the extensively exothermic process, so extreme caution should be used to avoid the spill of mercury**). Next, the as-prepared mercury-rich amalgam was dropped on sodium metals and spread on the surface. Since the alloying reaction was initialized immediately upon the contact of the two materials, the casting process should be as fast as possible to obtain a homogeneous amalgam layer.

Synthesis of sodium iron hexacyanoferrate (Fe-HCF): The Fe-HCF sample was synthesized via a simple citrate-assisted co-precipitation method as described elsewhere. Typically, 1.67 g (6 mmol) iron sulfate pentahydrate ($FeSO_4 \cdot 7H_2O$) and 5.0 g sodium citrate were dissolved in 100 mL deionized water. Next, 100 mL sodium ferrocyanide solution (1.69 g, 4 mmol) were slowly added to the above

solution under stirring. The mixture was stirred for 12 hrs. The white precipitates were then collected by centrifugation and vacuum-dried at 100 °C.

Physical characterization: X-ray diffraction (XRD) patterns were collected on a Rigaku Miniflex 600 desktop at 40 kV and 20 mA with a Cu Kα radiation (λ=1.54 Å). A Kapton@ film was used to protect the sample when performed the diffraction experiments. Scanning electron microscopy (SEM) studies were carried out on an FEI Verios 460L and high-resolution transmission electron microscopy (HR-TEM) images were acquired with an FEI Talos F200x at 200 kV. The TEM sample was prepared by sonicating the amalgam layer under inert atmosphere in PC. The supernatant was then dropped on a TEM grid and dried in an Ar-filled glove box for analysis.

Electrochemical evaluation: All cells were assembled in an Ar-filled glove box with O_2 and H_2O level below 0.1 ppm. Symmetric cells were assembled bare Na foil electrodes and/or amalgam-protected Na electrodes. Each electrode was 12 mm in diameter with an average thickness of 500 μm. The Fe-HCF electrodes were slurry-casted onto carbon-coated Al current collectors using 70 wt% active material, 20 wt% Super P carbon and 10 wt% poly(vinyl difluoride) (PVDF) with a typical loading of the active material of 1.0-1.5 mg cm^{-2}. Hard carbon electrodes were slurry-casted onto Cu current collectors using 80 wt% active material, 20 wt% Super P carbon and 10 wt% carboxymethyl cellulose (CMC) with a typical loading of the active material of 1.0-1.5 mg cm^{-2}. Coin-type (2032) cells were assembled using a glass fiber separator with electrolyte composed of 1.0 M sodium perchlorate ($NaClO_4$) in ethylene carbonate (EC) and propylene carbonate (PC) (1:1 vol/vol). Galvanostatic experiments were carried out on Land CT2001 cyclers at room temperature. Cyclic voltammetry (CV) was carried out on a VMP3 at 0.05 mV s^{-1} between 2.0-4.6 V. The electrochemical

impedance spectroscopy (EIS) measurements were conducted on a Princeton PARSTAT 2273. The frequency was ranged from 1 MHz to 0.01 mHz with an alternating voltage signal amplitude of 5 mV. In-situ optical microscopy studies: In-situ optical microscopy experiments were carried out with a Keyence VHX-950F microscope at room temperature. A home-made cell was used with a transparent glass to in-situ monitor the morphology evolution of the electrodes. The cells were assembled either by amalgam-protected anodes or pristine sodium anodes along with glass-fiber separators. The electrolyte was 1 M $NaClO_4$/PC+EC as in the coin cells.

Computational Methods

Computational details: First principles computations are performed using the DMol3 code.[S1] The Perdew, Burke, and Ernzerhof (PBE) exchange-correlation functional within a generalized gradient approximation (GGA) was employed. [S2] The double numerical plus polarization (DNP) was chosen as the basis set for other elements. During geometry optimizations, the K-points of Na (110) is set to be 2*2*1. The binding energies and different charge densities were calculated by subtracting the free energy and charge density of the substrate and Na atom from the Na-absorbed system, respectively. Molecular dynamic simulations were carried out by Large-scale Atomic/Molecular Massively Parallel Simulator (LAMMPS) [S3] with time-step of 0.5 fs in the NVT ensemble at 300 K. During the simulation, Na atoms was plated every 5 ps at a distance of greater than 10 Å above the Na-vacuum interface. The Na-Na[S4], Hg-Hg[S5] and Na-Hg[S6] interactions were parametrized according to the previous work.

SUPPLEMENTARY FIGURES

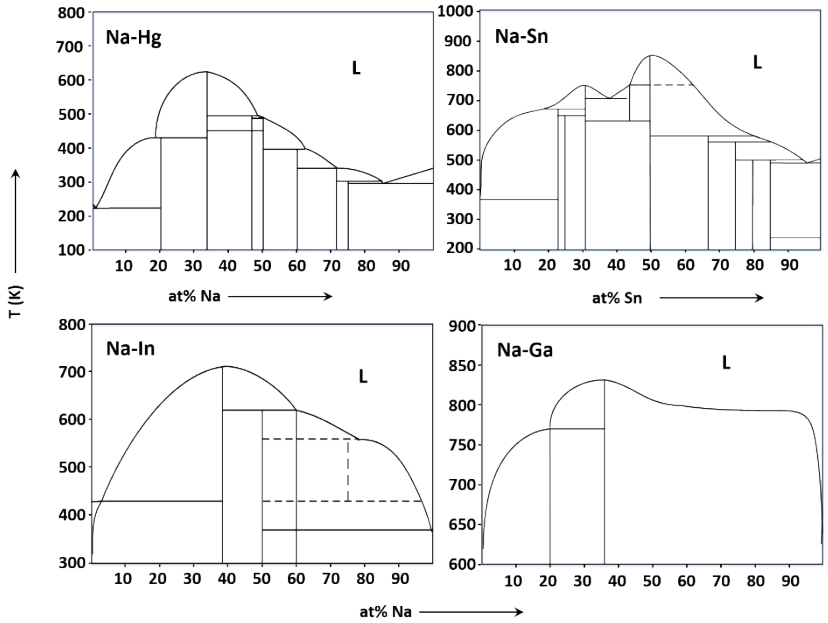

Figure S1. Phase diagrams of sodium with Hg, Sn, In and Ga.

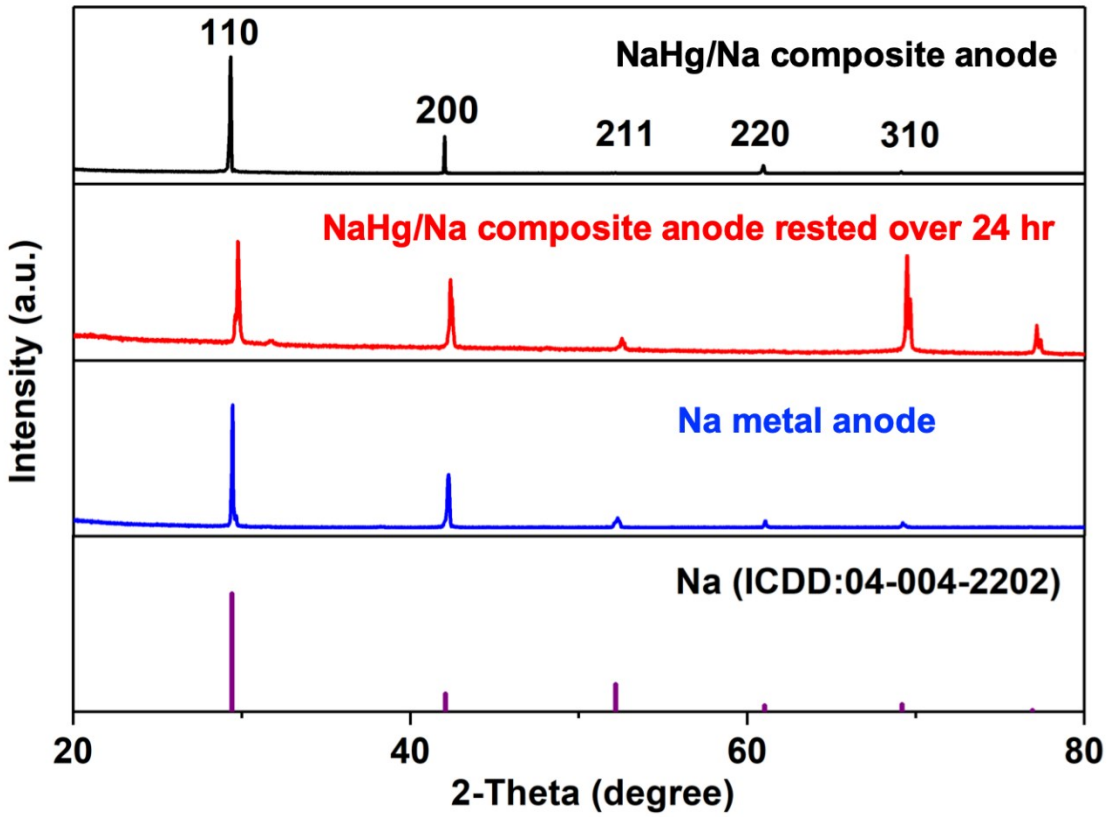

Figure S2. XRD patterns of Na and NaHg/Na composite anodes. The phase diagram suggests Na_3Hg (ICDD: 04-007-1890) can be formed at the sodium-rich regions. However, this intermetallic phase was not detected by XRD possibly due to the quasi-liquid nature of the amalgam coating. The extra peak at 31.4° cannot be identified to any known Na-Hg alloys (i.e., Na_3Hg and Na_5Hg_2) and sodium oxide/hydroxide. The sharply increased intensity of the [310] peak is possibly a result of sample displacement during the XRD measurement as the amalgam surface becomes rough after the resting process. Although the pattern has some variation, it is noticed the main phase is still from the metallic Na, indicating the quasi-liquid layer is relatively stable after 24-hr resting.

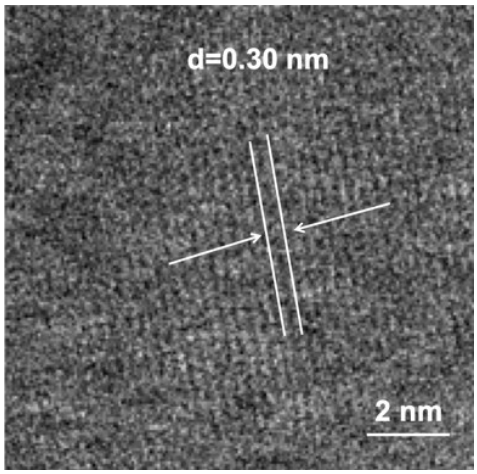

Figure S3. High-resolution TEM image showing the lattice fringes corresponding to the (110) diffraction of sodium.

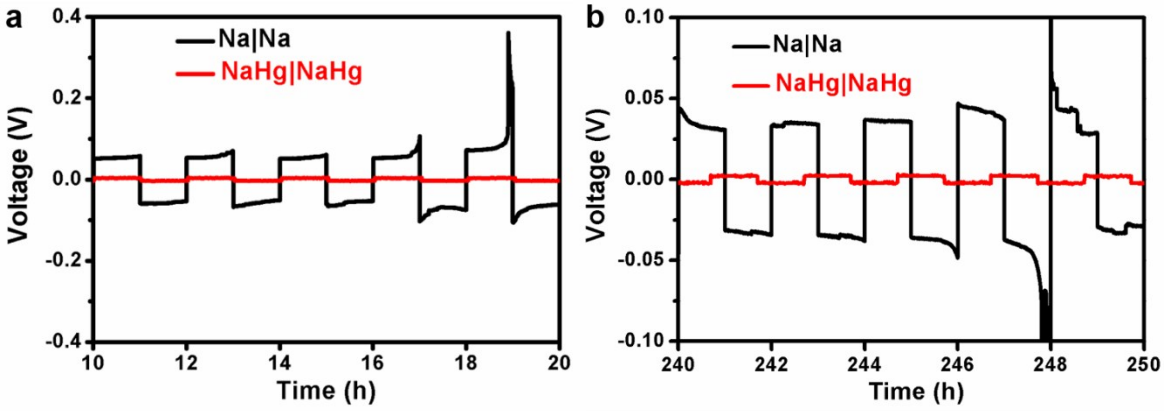

Figure S4. Voltage profiles of Na|Na and NaHg|NaHg symmetric cells at 2 $mAcm^{-2}$.

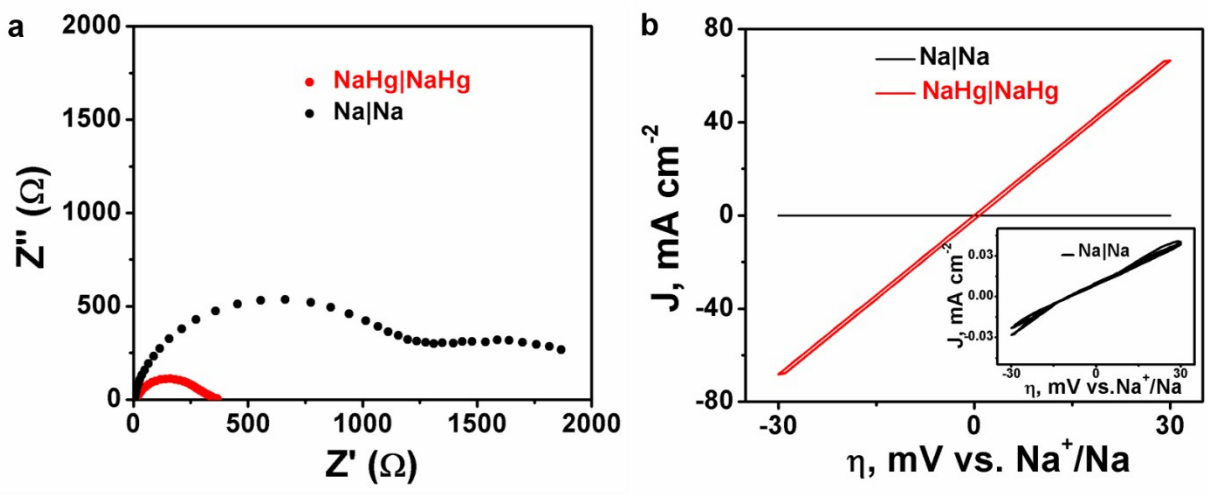

Figure S5. Electrochemical analyses of pristine sodium and protected electrodes in symmetric cells. a) EIS spectra. b) polarization curves.

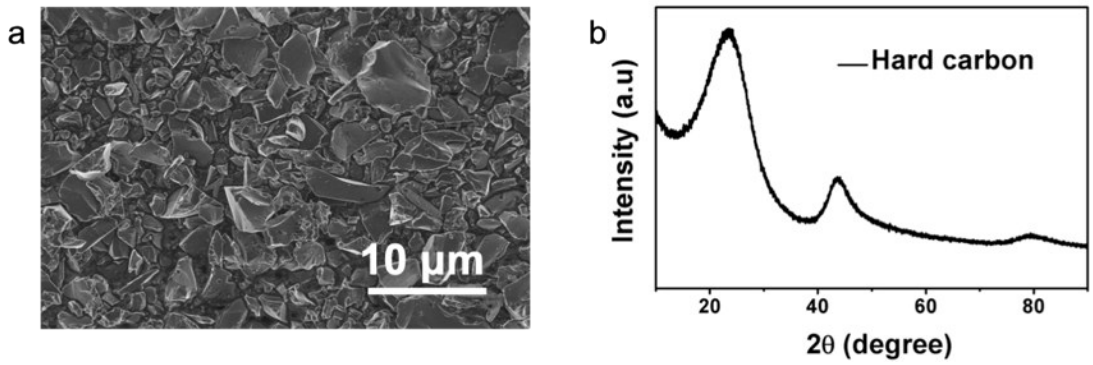

Figure S6. Physical characterizations of the commercial hard carbon. a) SEM image. **b)** XRD pattern.

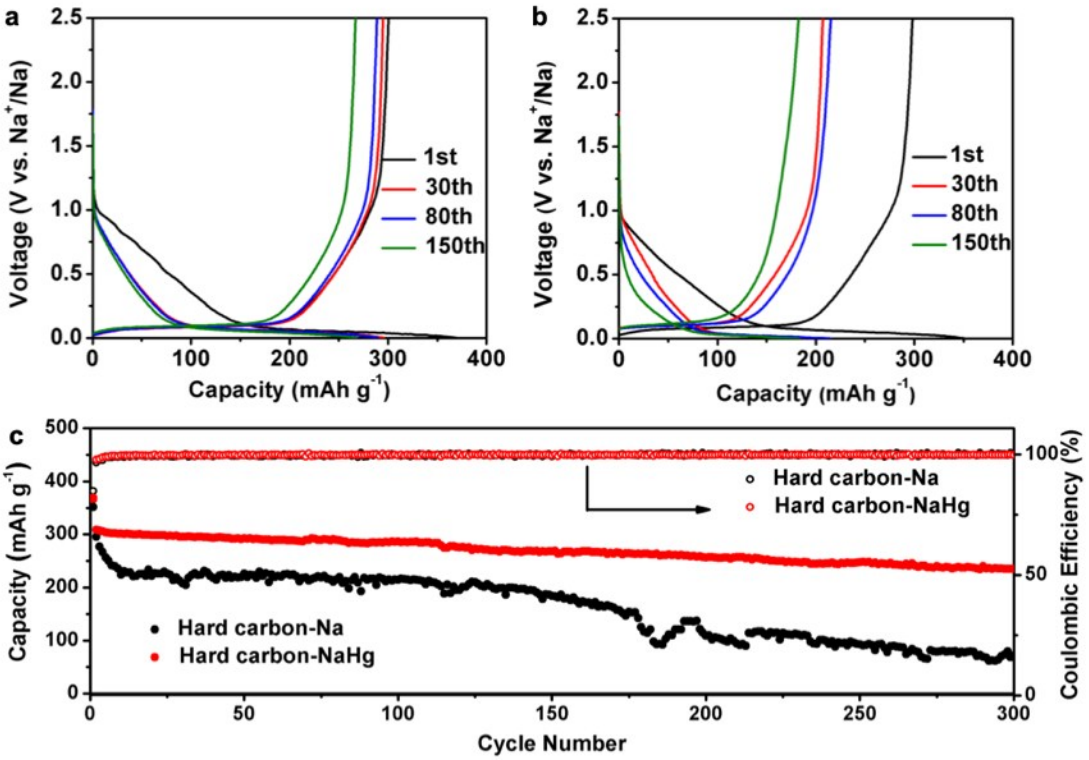

Figure S7. Full cell performance with commercial hard carbon counter electrodes. Voltage profiles of a) protected sodium anode and b) pristine sodium anode. **c)** Cycling performance at 50 mA g^{-1}.

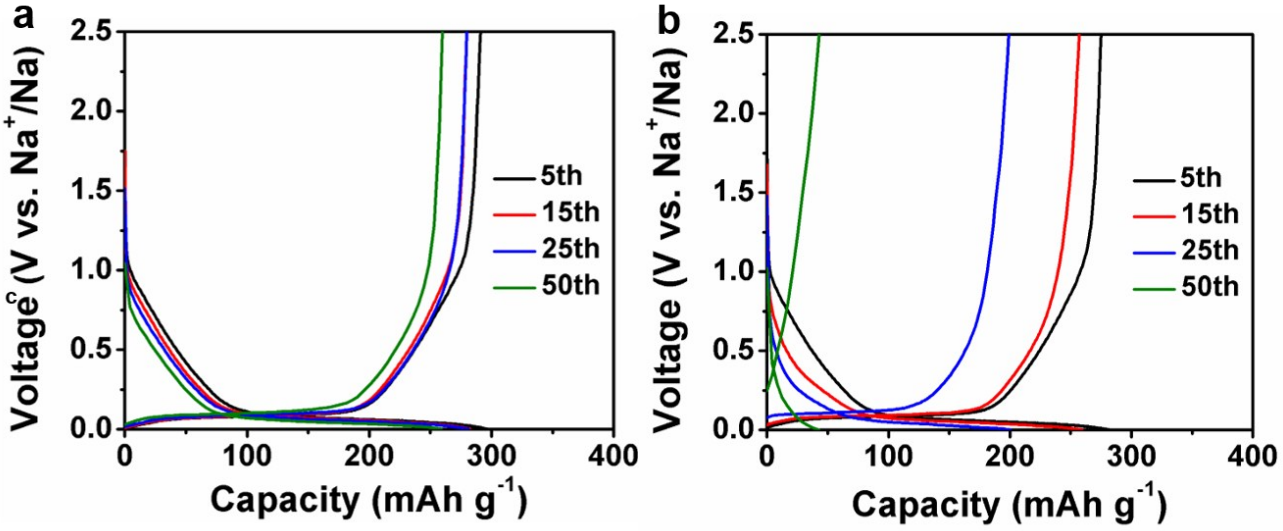

Figure S8 Voltage-capacity profiles of a) protected sodium anode and b) pristine sodium anode.

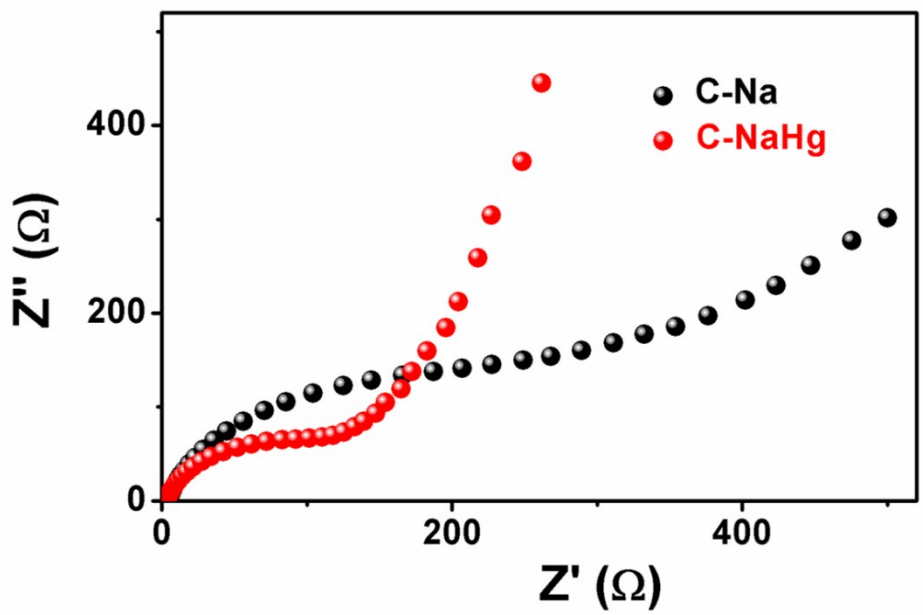

Figure S9. EIS spectra of prototype full cells assembled with pristine sodium and amalgam electrodes coupled with hard carbon counter electrodes.

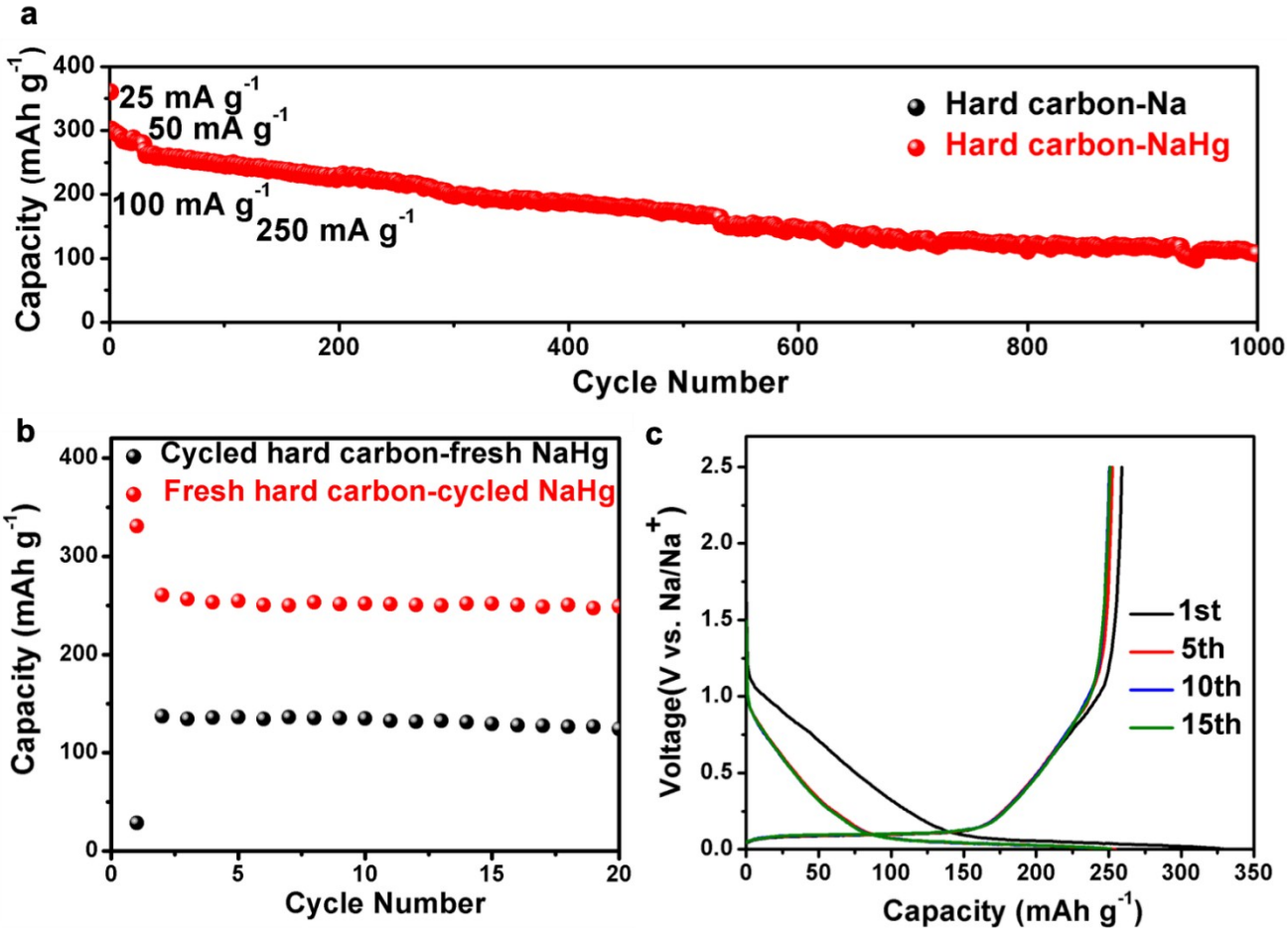

Figure S10. Analyses of cycled Na-Hg and hard carbon electrodes. a) Long-term cycling of protected sodium anode coupled with hard carbon electrode. **b)** Capacities of reassembled cells using cycled electrodes with fresh NaHg and hard carbon electrodes, respectively. **c)** Voltage-capacity profiles of the cell assembled using cycled NaHg and fresh hard carbon.

In order to clarify this unexpected capacity degradation after long-term cycling (Figure S10a), the cell was opened up and the two electrodes were re-assembled using fresh NaHg and hard carbon, respectively. In Figure S10b, the cell composed of cycled carbon has a small capacity of 120 mAh g^{-1}, whereas the cell composed of cycled NaHg almost resumes its high capacity around 250 mAh g^{-1} (Figure S10c). These results clearly demonstrate the long-term capacity fading noted above is actually due to the deterioration of the carbon electrode. This is easily understood because protected anodes exhibit excellent cycling at much higher current densities (>2 mA cm^{-2}) in half cells. Given that the average loading of the hard carbon electrodes is ~1 mg cm^{-2}, the maximum current density is only ~0.25 mA cm^{-2} in full cells, which has very little influence on the NaHg protected anode.

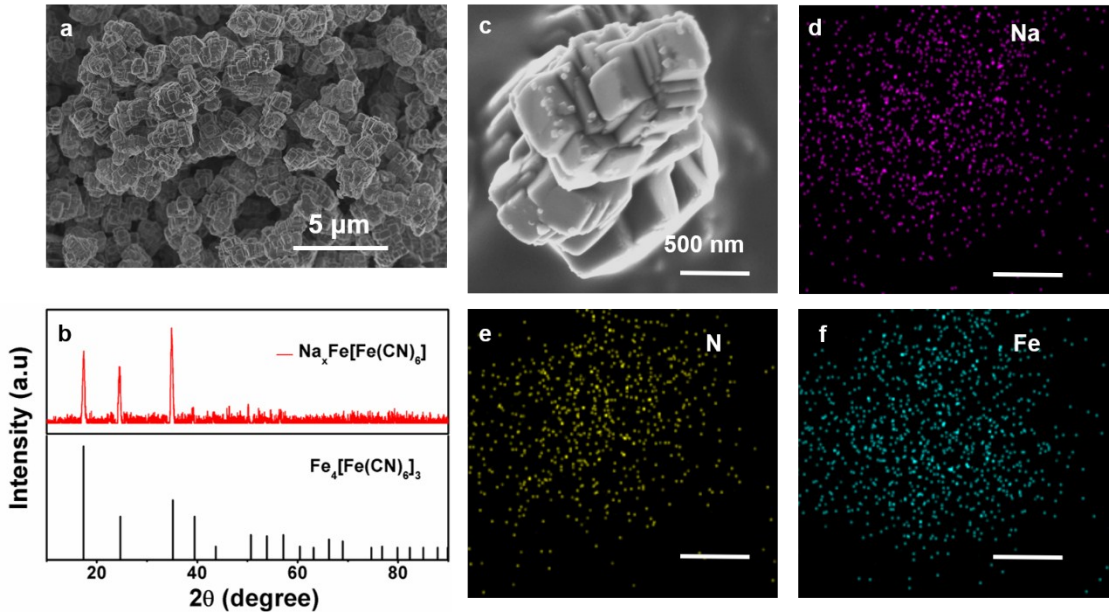

Figure S11. Physical characterizations of Fe-HCF cathode materials. a) SEM image. **b)** XRD pattern. **c-f)** STEM image and the corresponding elemental mapping of Na, Fe and N.

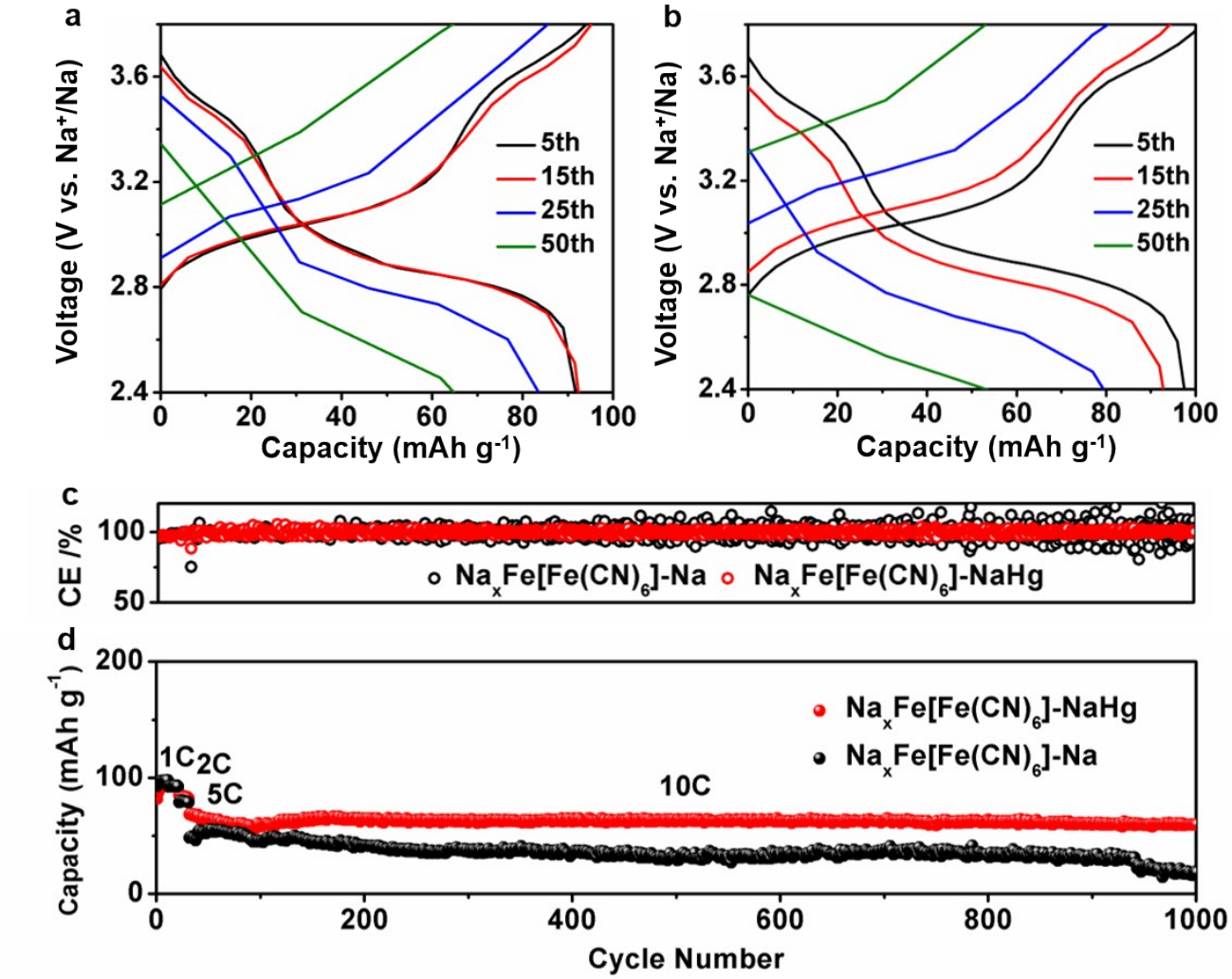

Figure S12. Electrochemical performance of Na and NaHg anodes coupled with Prussian blue cathodes. Voltage-capacity profiles of a) protected and b) pristine cells. **c, d)** Cycling behaviors of two cells at various current rates.

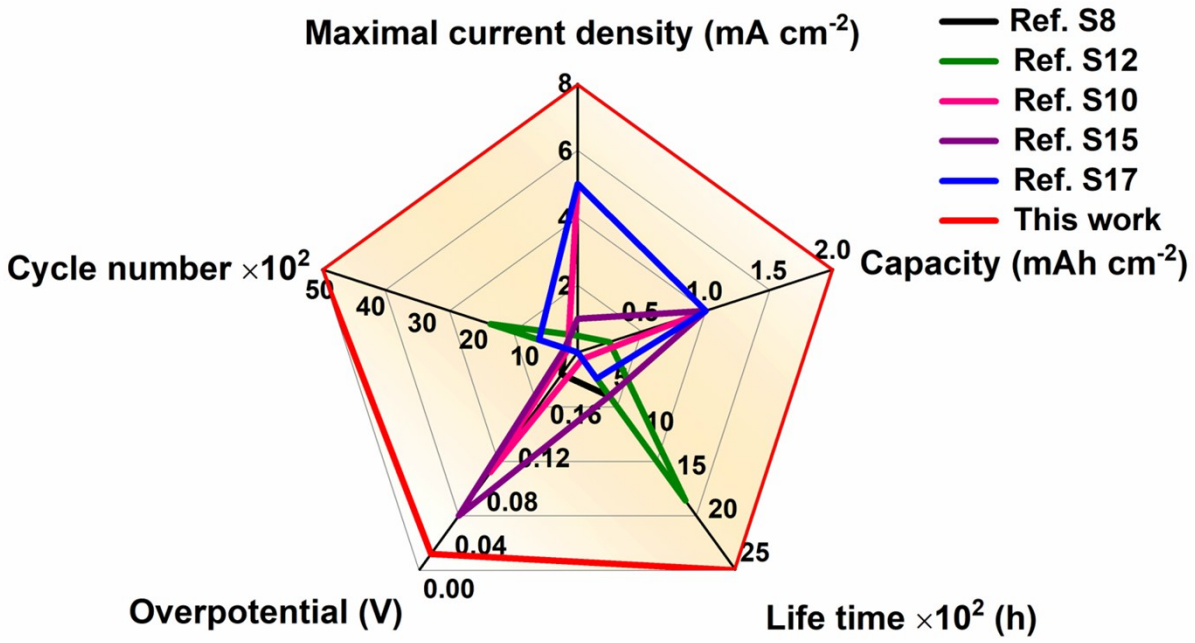

Figure S13. Performance comparison between this work and published studies.

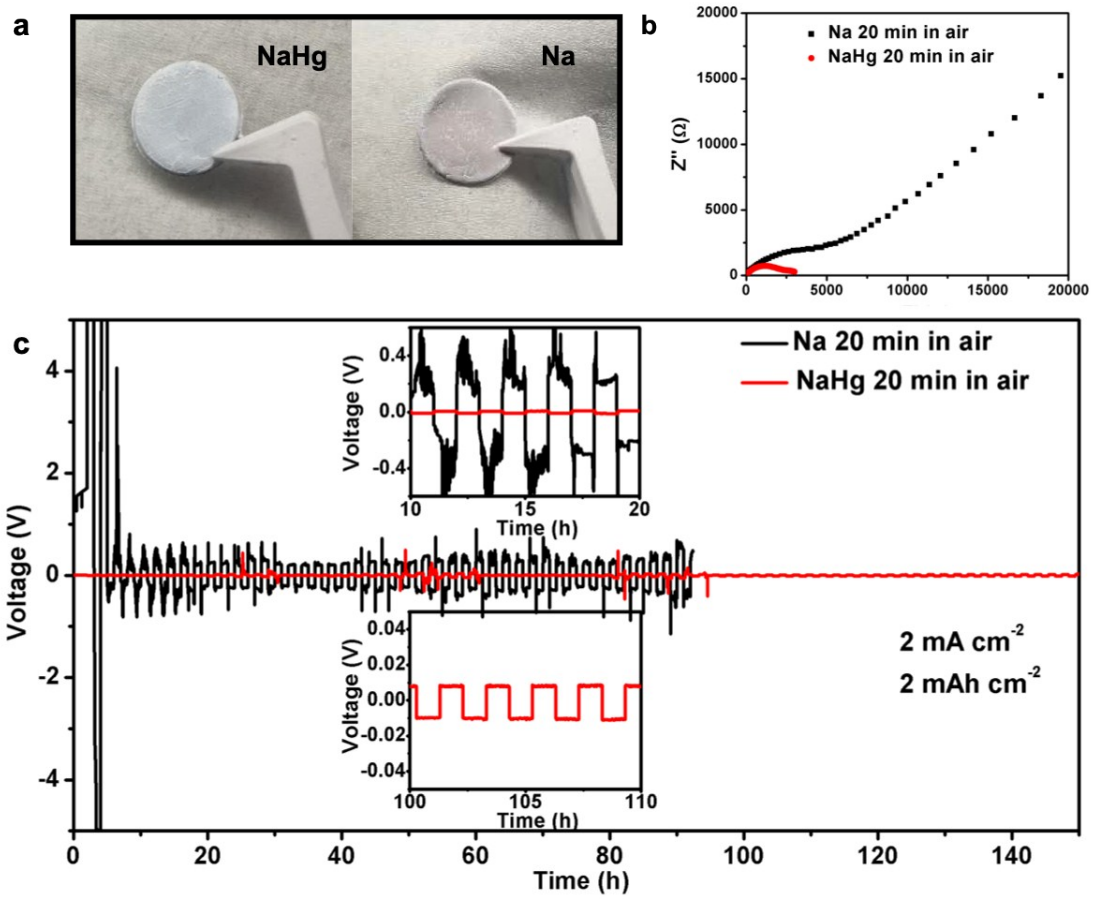

Figure S14. Dry air stability of the amalgam-protected sodium. a) Optical images of the protected and pristine sodium electrode after exposed in air for 20 mins. **b)** EIS spectra of the cells with the resulting amalgam and pristine sodium anodes. **c)** Voltage and cycling profiles of the cells with a plating capacity of 2 mAh cm^{-2} at 2 mA cm^{-2}.

The air stability of the amalgam-protected sodium anodes was examined by exposing the anodes in air (RH of ~10%) for 20 min. The optical images show fast oxidation of the pristine sodium, causing greatly increased impedance. The symmetric cell with such oxidized electrodes displays very large and unstable overpotentials as additional activation energy is required for Na-ions to penetrate the passivation layer. In contrast, the amalgam anode shows significantly reduced overpotentials of ~100 mV.

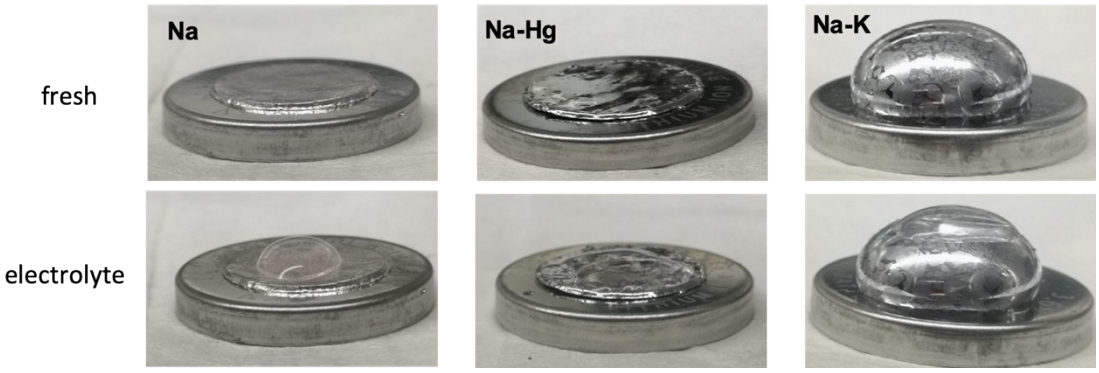

Figure S15. Comparison of the wettability between Na, Na-Hg, Na-K alloys and the electrolyte.

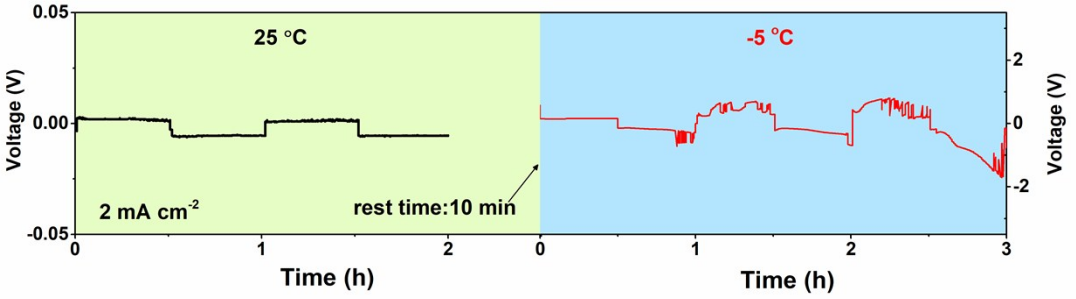

Figure S16. Temperature influence on the performance of amalgam-protected anodes.

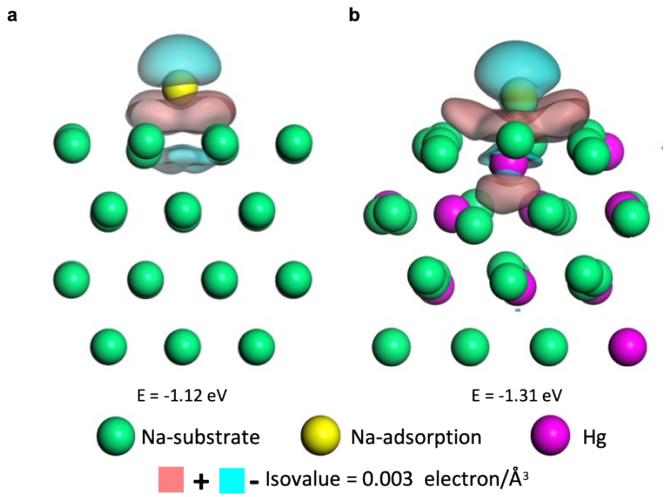

Figure S17. Comparison of surface energy. Differences of charge densities for Na on a) Na (110) and b) Hg-doped Na (110) surfaces and their corresponding binding energies. The blue and red regions represent the deletion and accumulation of electrons, respectively.

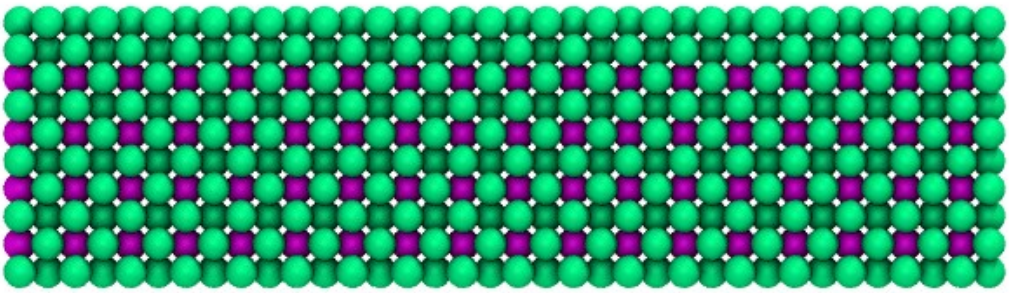

Figure S18. The pristine model of $NaHg_{0.2}$ alloy surface. Hg atoms were embedded among the Na lattice, and the Hg fraction was set to ~20 % to match the experimental results.

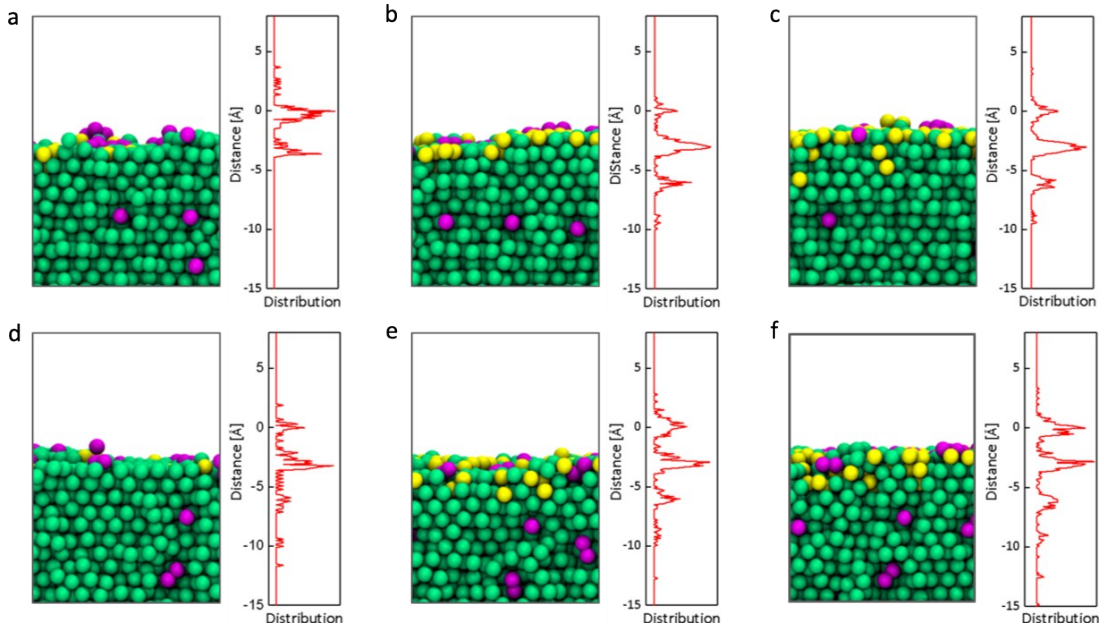

Figure S19. Molecular dynamic illustration of Na plating behaviors. a)-c) Na plating and diffusion on/in $NaHg_{0.015}$ amalgam alloy. **d)-f)** Na plating and diffusion on/in $NaHg_{0.03}$ amalgam alloy. The simulations show the sodium structure is roughly maintained with such small amounts of Hg atoms.

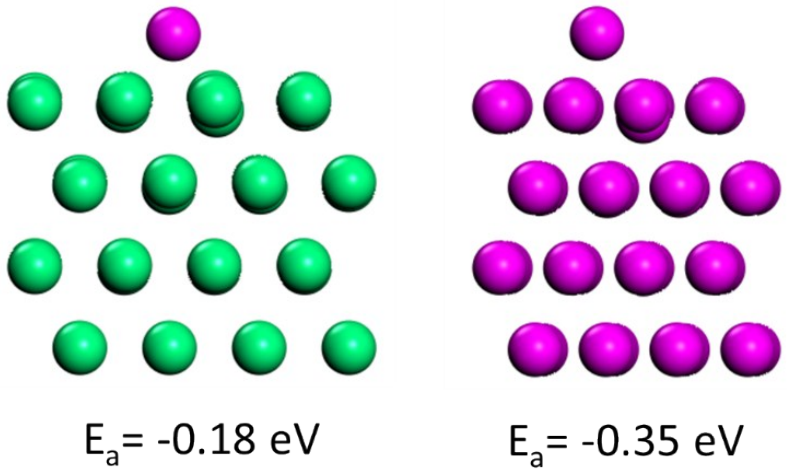

Figure S20. Structure and adsorption energy of Hg atoms adsorbed on the Na (110) and Hg (110) surfaces.

Video 1. Alloying process by dropping Na_xHg_{1-x} (x = 0, 0.01 and 0.1) onto Na metal foil.

Video 2. Alloying process by placing P, Ga, In and Sn onto Na metal foil.

Video 3. Dissolution of Na-Hg amalgam anode in ethanol for mercury recycling.

The recycling ability of batteries and electrodes has attracted much attention to minimize the disposal of hazards to the environment. This is particularly important for the mercury-involved amalgam anodes. The efficient collection and recycling of mercury would greatly promote the prospect of its commercial applications. Thereby, an amalgam anode was examined in ethanol to attempt the separation of sodium and mercury. As expected, the sodium-rich amalgam anode reacted with ethanol instantly as evidenced by the fast outgassing in the first several minutes. The reaction was gradually slowed down due to the consumption of sodium in the alloy, and eventually the bubbles disappeared after 24 hrs, leaving a mercury drop on the bottom of the container. This experiment suggest mercury can be collected from the amalgam simply by dissolving sodium at room temperature without involving any complicated procedures. This efficient recycling process is beneficial to protect the environment from the wasted batteries and significantly reduce the cost to fabricate amalgam anodes by the facile collection of mercury. Nonetheless, the handle and usage of the amalgam anodes should be careful, and protocols must be established for the production of electrodes and cells as well as the recycling of batteries after use.

SUPPLEMENTARY TABLE

Table S1. Summary of the representative works on sodium metal anodes.

Protection	Current density (mA cm^{-2})	Capacity (mAh cm^{-2})	Life time（h）	References
PEALD Al_2O_3[S7]	0.25	1	400	*Adv. Energy Mater.*, 2017, **7**, 1601526.
	0.5	1	120	
Na-wood[S8]	1	1	500	2017, **17**, 3792.
	0.5	0.25	250	
NaBr coating[S9]	0.25	0.25	250	*Nat. Commun.*, 2017, **8**, 898.
	0.5	0.5	250	
ALD Al_2O_3[S10]	3	1	500	*Adv. Mater.*, 2017, **29**, 1606663.
	5	1	75	
MLD alucone[S11]	3	1	120	*Nano Lett.*, 2017, **17**, 5653.
Sn–Na[S12]	0.5	0.25	1700	*Nat. Energy*, 2018, **3**, 310.
Na_2S_6[S13]	10	5	100	*Angew. Chem. Int. Ed.*, 2018, **57**, 7734.
	10	1	80	
	5	3	120	
Multilayer graphene[S14]	1 (7 layers)	1	200	*Nano Lett.*, 2017, **17**, 6808.
NSCNT[S15]	1	1	500	*Adv. Mater.*, 2018, **30**, 1801334.
Na@r-GO[S16]	1	1	600	*Angew. Chem. Int. Ed.*, 2017, **56**, 1192.
Na/C composite[S17]	3	2	150	*Adv. Energy Mater.*, 2018, **8**, 1702764.
3DHS[S18]	0.5	1	1350	*Sci. Adv.*, 2019, **5**, eaau6264.
	1	1	370	
Na-K[S19]	80	16	1200	*Energy Environ. Sci.*, 2019, **12**, 1989.
Na-rich amalgam	**2**	**2**	**1400**	**This work**
	4	**4**	**240**	
	8	**2**	**5000**	
	8	**8**	**240**	

Supplementary References:

S1 B. Delley, *J. Chem. Phys.*, 2000, **113**, 7756-7764.

S2 J. P. Perdew, K. Burke and M. Ernzerhof, *Phys. Rev. Lett.*, 1996, **77**, 3865-3868.

S3 S. Plimpton, *J. Comput. Phys*., 1995, **117**, 1-19.

S4 A. Nichol and G. J. Ackland, *Phys. Rev. B*, 2016, **93**, 184101.

S5 X. W. Zhou, D. K. Ward, J. E. Martin, F. B. van Swol, J. L. Cruz-Campa and D. Zubia, *Phys. Rev. B*, 2013, **88**, 085309.

S6 U. Buck and H. Pauly, *J. Chem. Phys.*, 1971, **54**, 1929-1936.

S7 W. Luo, C.-F. Lin, O. Zhao, M. Noked, Y. Zhang, G. W. Rubloff and L. Hu, *Adv. Energy Mater.*, 2017, **7**, 1601526.

S8 W. Luo, Y. Zhang, S. Xu, J. Dai, E. Hitz, Y. Li, C. Yang, C. Chen, B. Liu and L. Hu, *Nano Lett.*, 2017, **17**, 3792-3797.

S9 S. Choudhury, S. Wei, Y. Ozhabes, D. Gunceler, M. J. Zachman, Z. Tu, J. H. Shin, P. Nath, A. Agrawal, L. F. Kourkoutis, T. A. Arias and L. A. Archer, *Nat. Commun.*, 2017, **8**, 898.

S10 Y. Zhao, L. V. Goncharova, A. Lushington, Q. Sun, H. Yadegari, B. Wang, W. Xiao, R. Li and X. Sun, *Adv. Mater.*, 2017, **29**, 1606663.

S11 Y. Zhao, L. V. Goncharova, Q. Zhang, P. Kaghazchi, Q. Sun, A. Lushington, B. Wang, R. Li and X. Sun, *Nano Lett.*, 2017, **17**, 5653-5659.

S12 Z. Tu, S. Choudhury, M. J. Zachman, S. Wei, K. Zhang, L. F. Kourkoutis and L. A. Archer, *Nat. Energy*, 2018, **3**, 310-316.

S13 H. Wang, C. Wang, E. Matios and W. Li, *Angew. Chem. Int., Ed.*, 2018, **57**, 7734-7737.

S14 H. Wang, C. Wang, E. Matios, W. Li, *Nano Lett.*, 2017, **17**, 6808-6815.

S15 B. Sun, P. Li, J. Zhang, D. Wang, P. Munroe, C. Wang, P. H. L. Notten and G. Wang, *Adv. Mater.*, 2018, **30***,* 1801334.

S16 A. Wang, X. Hu, H. Tang, C. Zhang, S. Liu, Y. W. Yang, Q. H. Yang and J. Luo, *Angew. Chem. Int. Ed.*, 2017, **56**, 11921-11926.

S17 S.-S. Chi, X.-G. Qi, Y.-S. Hu and L.-Z. Fan, *Adv. Energy Mater.*, 2018, **8**, 1702764.

S18 M. Zhu, S. Li, B. Li, Y. Gong, Z. Du and S. Yang, *Sci. Adv.*, 2019, **5**, eaau6264.

S19 L. Zhang, S. Peng, Y. Ding, X. Guo, Y. Qian, H. Celio, G. He and G. Yu, *Energy Environ. Sci.*, 2019, **12**, 1989-1998.